Peer-reviewed version available at *Catalysts* **2018**, *8*, 185; doi:10.3390/catal8050185

Article

Pyrene-based Conjugated Polymer/Bi_2MoO_6 Z-scheme Hybrids: Facile Construction and Sustainable Enhanced Photocatalytic Performance in Ciprofloxacin and Cr(VI) Removal under Visible Light Irradiation

Xianglong Yang [1,2], Yonggang Xiang[1], Xuepeng Wang[1], Shu Li[1], Hao Chen[1,2] and Xing Ding[1,*]

[1] College of Science, Huazhong Agricultural University, Wuhan 430070, China; xianglongyang@foxmail.com (X.L.Y.); ygxiang@mail.hzau.edu.cn (Y.G.X.); wangxuepeng@webmail.hzau.edu.cn (X.P.W.); 294124004@qq.com (S.L.); hchenhao@mail.hzau.edu.cn (H.C.)
[2] Key Laboratory of Environment Correlative Dietology, Ministry of Education, Wuhan 430070, China
* Correspondence: dingx@mail.hzau.edu.cn (X.D.); Tel.: +86-27-8728 8246

Abstract: Search for appropriate materials with favorable staggered energy band arrangements is important and of great challenge to fabricate Z-scheme photocatalysts with high activity in visible light. In this study, we demonstrated a facile and feasible strategy to construct highly active organic-inorganic Z-scheme hybrids (P-BMO) with linear pyrene-based conjugated polymer (P17-E) and Bi_2MoO_6 via in-situ palladium-catalyzed cross-coupling reaction. Characterization results revealed C-O chemical bond formed at the heterointerface between P17-E and Bi_2MoO_6 after in-situ polycondensation and endowed the hybrids with observably improved photogenerated carries transfer capability. Visible light driven photocatalytic removal of ciprofloxacin and Cr(VI) were significantly enhanced after the incorporation of P17-E into Bi_2MoO_6 whether with the morphology of nanosheets, nanobelts or microspheres. Moreover, this P-BMO hybrids were also found to exhibit sustainable excellent photocatalytic performance after four runs of photocatalytic evaluation test, suggesting its high activity and stability. To better eliminate the redox ability enhancement of P-BMO, a reasonable Z-scheme electrons transferring mechanism between P17-E and Bi_2MoO_6 was proposed and proved by the determination of $\bullet O_2^-$ and $\bullet OH$ and Pt nanoparticles photodeposition experiments. This work might provide a viable source and insight into the design of Z-scheme photocatalysts with excellent redox ability for environmental remediation.

Keywords: Photocatalysis; Z-scheme; conjugated polymer; Bi_2MoO_6

1. Introduction

As a trustworthy technique to harvest solar light for environmental remediation, photocatalysis has been widely utilized in removal of antibiotics and heavy metals by virtue of its sustainable, economical and environmentally benign properties [1-4]. To acquire suitable photocatalysts with broad photo absorption, fast charge transportation and efficient surface reactions, several commonly used techniques have been explored, such as sensitization, doping, fabrication of heterojunction, surface engineering and so on [5-9]. Among them, the fabrication of Z-scheme hybrids is recognized to be extraordinarily attractive, since it can enormously extend the light absorption region and accelerate the separation of e^-/h^+ pairs as well [10-12]. Meanwhile, the recombination of carriers between two components can also liberate the conduction band (CB) and valence band (VB) with stronger redox ability, thus endowing the hybrids with efficient surface reactions [11, 13]. For instance, a direct Z-scheme photocatalyst with the $W_{18}O_{49}/g\text{-}C_3N_4$ heterostructure reported by Zhang

Peer-reviewed version available at Catalysts 2018, 8, 185; doi:10.3390/catal8050185

et al. was found to possess almost a full-spectrum-driven photocatalytic activity for highly efficient H_2 evolution [14]. Hong et al. explored V_2O_5 decorated g-C_3N_4 as Z-scheme photocatalyst for efficient environmental purification [15]. Furthermore, Li et al. synthesized Z-scheme Bi_2MoO_6/MO (M = Cu, $Co_{3/4}$, or Ni) hybrids with enhanced photocatalytic performance toward organic degradation [16]. However, limited by the intrinsic band-gap and corresponding band potentials of conventional semiconductors, it's still of great challenge to seek out appropriate materials with favorable staggered energy band arrangements to fabricate highly active Z-scheme photocatalysts.

Recently, conjugated polymers (CP), consisting of π-electron conjugated structure, have emerged as a functional organic semiconductor because of its marvelous photoelectrochemical activity and charge carriers mobility [17-19]. Besides the traditional utilizations in light-driven organic synthesis and organic photovoltaics, CP have also revealed fantastic performances in photocatalysis, such as poly(diphenylbutadiyne) for pollutants degradation, polybenzothiadiazoles for H_2 evolution and poly(dibenzo[*b*,*d*]thiophene 5,5-dioxide) for NO oxidation [20-24]. In addition, unlike the conventional semiconductors, its HOMO and LUMO potentials can be fine-tuned through varying the monomers or adjusting the molecular structures [25, 26], implying that CP might be an ideal candidates for constructing Z-scheme hybrids, which has been confirmed by our previous studies. [27, 28]. However, the heterocycles structure in CP gave rise to their poor stabilities during the photocatalytic process. Accordingly, we further explored a new linear pyrene-based conjugated polymer (P17-E) without heteroatom, which exhibited high activity and stability in H_2 evolution [29]. This linear conjugated polymer is expected to be a better substitute in construction of Z-scheme hybrids with superior stability and activity.

For confirmation, visible-light responsive Bi_2MoO_6 was selected as the model semiconductor to construct hybrid photocatalysts with P17-E, in view of its suitable band positions, and layered structure (characterized by $[Bi_2O_2]^{2+}$ slabs interleaved with double layers of perovskite-like $[MoO_4]^{2-}$) [30, 31]. What's more, various Bi_2MoO_6 based catalysts have been synthesized and applied in environmental remediation and CO_2 photoreduction so far [32-34]. But constrained by the intrinsic band-gap and charge carriers mobility of Bi_2MoO_6, the quantum efficiencies of these materials still need to be further strengthened [35, 36]. Herein, the Z-scheme hybrids (P-2BMO) were firstly fabricated through the cross-coupling reaction of 1,6-Dibromopyrene and 1,4-diethynylbenzene on the surface of Bi_2MoO_6 nanosheets. Extensive characterizations were employed to investigate the crystallinity, morphology, chemical states and optical property of the hybrids. Photocatalytic removal of ciprofloxacin and Cr(VI) under visible light irradiation were utilized to evaluate the photocatalytic activity of these novel organic-inorganic hybrids. Moreover, to evaluate the applicability of the method for constructing Z-scheme photocatalysts, 6.7% P-1BMO and 6.7% P-3BMO hybrids were further fabricated using Bi_2MoO_6 nanobelts and microspheres, respectively. And their photocatalytic activity was also investigated and compared with the pristine P17-E and Bi_2MoO_6. Finally, based on systematical measurements including photoelectrochemical tests and determination of reactive species, a reasonable Z-scheme mechanism was proposed and verified by a series of credible techniques, including the NBT photodegradatio, terephthalic acid (TA) photo-luminescence probing technique and Pt nanoparticles photodeposition experiment [37-39]. This work taking different dimensional Bi_2MoO_6 as the model materials, provides an available strategy to construct Z-scheme organic-inorganic hybrid photocatalysts with enhanced photocatalytic performance.

2. Results and Discussion

2.1 Characterization of the samples

The crystalline and morphologic properties of the hybrids are illustrated by XRD and TEM analysis (Figure 1). As shown in Figure 1a, the sharp diffraction peaks in the XRD pattern of 2BMO can be readily assigned to the orthorhombic phase of Bi_2MoO_6 (JCPDS card no. 76-2388), indicating its high quality of crystallinity [30]. P17-E is found to be amorphous with broad and low peaks, which is common in conjugated polymers. Compared to the pristine Bi_2MoO_6 nanosheets, no significant change in the XRD patterns of P-2BMO hybrids can be observed, indicating the incorporation of P17-E made no difference on the crystal structure of 2BMO. TEM images in Figure 1b, c demonstrate that the pristine 2BMO and P17-E are composed of homogeneous nanosheets and agglomerate flakes, respectively. After introducing P17-E to the surface of Bi$_2$MoO$_6$ nanosheets, some nonspecific flakes can be observed in the TEM image of 6.7% P-2BMO (Figure 1d), indicating intimate contact occurs in the hybrid photocatalyst. In addition, the hybrids are observed to have legible orthorhombic lattice fringes with space of 0.274 nm and 0.275 nm (inset in Figure 1d), corresponding to the (002) and (200) planes of Bi$_2$MoO$_6$. And the coverture layer without lattice fringe can be thought as the P17-E attached to the Bi$_2$MoO$_6$.

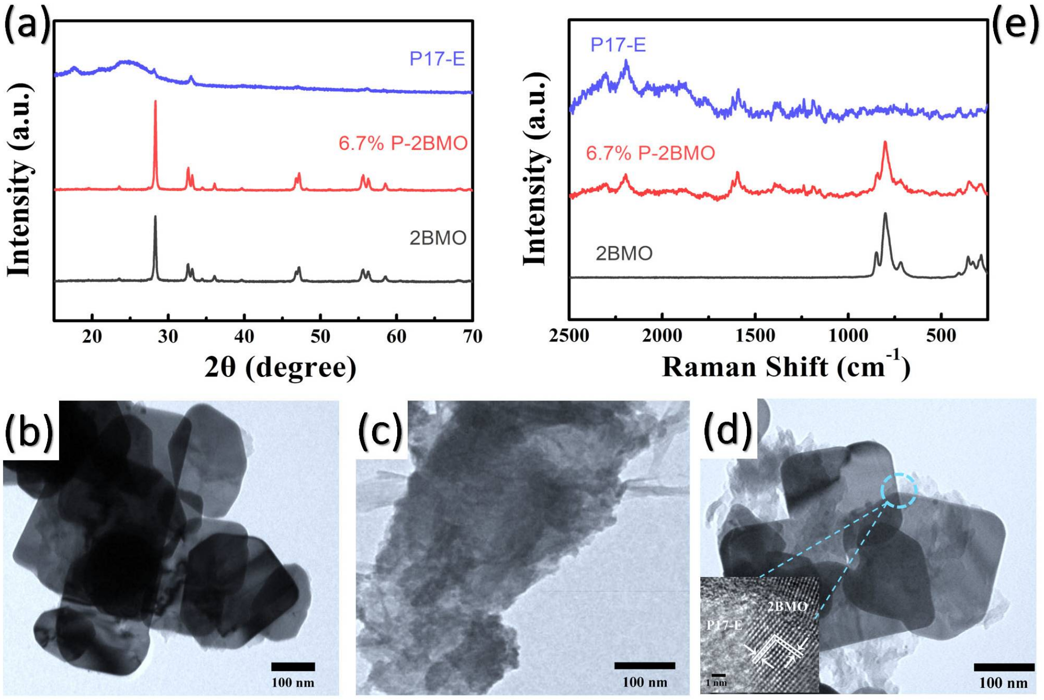

Figure 1. (**a**) XRD patterns of 2BMO, 6.7% P-2BMO and P17-E; TEM images of (**b**) 2BMO, (**c**) P17-E and (**d**) 6.7% P-2BMO, inset shows the corresponding HRTEM images; (e) Raman spectra of 2BMO, 6.7% P-2BMO and P17-E.

For better confirmation on the successful introduction of P17-E on Bi$_2$MoO$_6$, Raman spectroscopy was first conducted to investigate the structure of the as-prepared samples (Figure 1e). Peaks at 1362 cm^{-1}, 1537 cm^{-1} and 2204 cm^{-1} in pure P17-E are identified as ring stretch, C=C stretch and C≡C stretch, respectively [40]. For pristine Bi$_2$MoO$_6$ nanosheets, peaks around 805 cm^{-1} with two shoulders at 722 and 852 cm^{-1} are indexed to the stretching modes of Mo-O bond and the ν_1 (A1g) vibration for distorted MoO$_6$ octahedron, respectively. Peaks between 270 and 360 cm^{-1} are corresponding to the different bending modes of MoO$_6$ octahedral unit [41]. As for P-2BMO hybrid, all peaks above were observed, while the corresponding Bi$_2$MoO$_6$ Raman peaks intensity became weaker after the coating of P17-E on its surface, supporting the joint combination of P17-E and Bi$_2$MoO$_6$. This was further confirmed by FT-IR analysis, in which the characteristic peak at 2200 cm^{-1} corresponding to the C≡C stretching mode was found in both pure P17-E and P-2BMO (Figure S1). XPS measurement was subsequently applied to investigate the chemical states and compositions of the hybrids. The typical XPS survey spectra of P17-E, 2BMO and 6.7% P-2BMO in Figure 2a illustrate the existences of Bi, Mo, O, and C in 6.7% P-2BMO. And their corresponding high resolution Bi 4f, Mo 3d, O1s and C 1s spectra were compared meticulously to gain a deep insight into the interaction between P17-E and Bi$_2$MoO$_6$. No obvious change can be observed in the Bi 4f and Mo 3d spectra of 2BMO and 6.7% P-2BMO (Figure S2a, b), in which the peaks at 158.7 and 164.0 eV are ascribed to Bi 4f$_{3/2}$ and Bi 4f$_{5/2}$, while peaks at 235.1 and 232.0 eV are attributed to Mo 3d$_{3/2}$ and Mo 3d$_{5/2}$,

Peer-reviewed version available at Catalysts 2018, 8, 185; doi:10.3390/catal8050185

respectively [42]. For O 1s and C 1s spectra in Figure 2b, c, new peaks at 532.3 eV of O 1s and 288.0 eV of C 1s are observed in 6.7% P-2BMO compared to the pure Bi_2MoO_6 and P17-E, which can be ascribed to the formation of C-O bond between P17-E and Bi_2MoO_6 [43,44]. Based on the characterizations all above, it can be inferred that the conjugated polymer P17-E is tightly integrated with Bi_2MoO_6 nanosheets through the formation of C-O chemical bond at the heterointerface after in-situ polycondensation rather than physical mixture, which might be in favor of electrons migration between P17-E and Bi_2MoO_6.

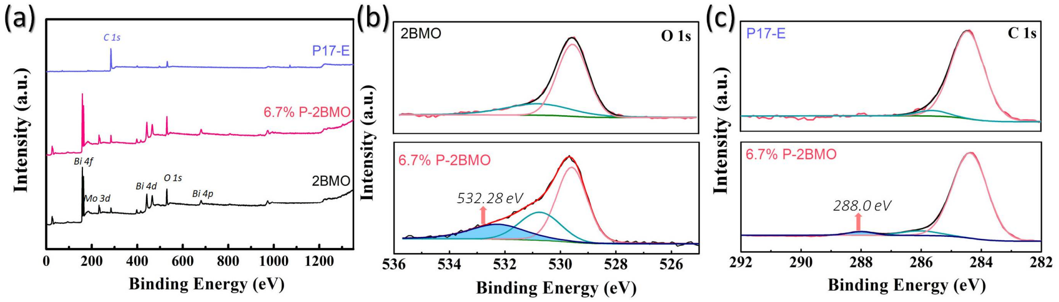

Figure 2. XPS spectra of 2BMO, 6.7% P-2BMO and P17-E: (**a**) survey spectra, (**b**) O1s and (**c**) C1s.

2.2 Photocatalytic performance of P-2BMO

Ciprofloxacin, as a broad-spectrum antibiotic agent, which neither absorbs visible light nor has a sensitization effect, was selected to evaluate the photocatalytic performance of the catalysts [45]. The CIP photodecomposition efficiency over P-2BMO hybrids with different weight ration were firstly estimated to investigate the effects of P17-E content on the photocatalytic activity. As shown in Figure 3a, all the P-2BMO composites exhibit much higher photocatalytic performance than the pristine P17-E and Bi_2MoO_6 nanosheets, and the corresponding kinetic parameters were calculated and summarized in Figure 3b. Interestingly, the photodegradation efficiency shows an obvious improvement when the P17-E loading level enhance from 0 to 6.7%, and then goes downhill upon further increase of P17-E proportion. The 6.7% P-2BMO composite, with a real content of about 5.9% (Figure S3), possesses the maximum rate constant of 0.034 min^{-1}, which is almost 17 times and 5 times as high as that of pure P17-E and Bi_2MoO_6 nanosheets, respectively. Obviously, the optimal proportion of P17-E for P-2BMO hybrids synthesis was determined to be 6.7%, since excessive conjugated polymer (more than 6.7%) may impair the formation of the effective heterointerface, hamper the photoinduced carriers transfer and thus restrain the photocatalytic performance. As expected, besides the superior photocatalytic capability, the 6.7% P-2BMO hybrids also exhibited high stability (Figure 3c). No obvious decrease of the photocatalytic activity can be observed even after four recycling runs. Similar to the photodecomposition of CIP, the tests of Cr(VI) photoreduction were also carried out to evaluate the photoreductive performance of the samples. As shown in Figure 3d, in comparison with the pristine 2BMO and P17-E, the P-2BMO hybrid exhibits much higher photocatalytic reduction ability in toxic Cr(VI) removal within 50 min. All these results demonstrated that the incorporation of P17-E into inorganic semiconductor (Bi_2MoO_6) can strengthen both the photodegradation and photoreduction activity of Bi_2MoO_6. That is to say, it's feasible to synthesis highly active organic-inorganic composites in the existence of linear conjugated polymer P17-E.

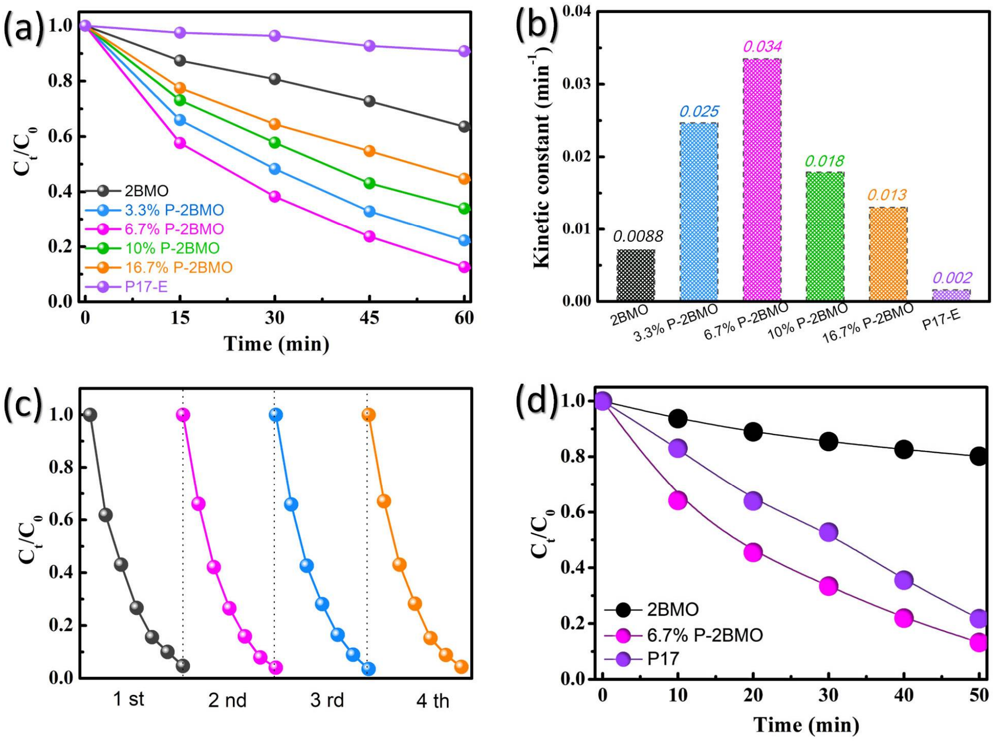

Figure 3. (**a**)Photodegradation of ciprofloxacin over various photocatalysts under visible light irradiation; (**b**)corresponding rate constants over different photocatalysts; (**c**) cycling runs for ciprofloxacin degradation over 6.7% P-2BMO and (**d**) photoreduction of Cr(VI) over 2BMO, 6.7% P-2BMO and P17-E under visible light irradiation.

2.3 Strategy Evaluation

To evaluate the applicability of the strategy for constructing highly active photocatalysts, we further synthesized 6.7% P-1BMO and 6.7% P-3BMO using Bi_2MoO_6 nanobelts and microspheres, respectively. As shown in Figure S4-8, systematic characterizations including XRD, TEM, FT-IR, Raman and TG demonstrated that the P17-E was also successfully introduced to the surface of 1BMO and 3BMO via the cross-coupling reaction. What's more, their photocatalytic performance was checked and displayed in Figure S9. Obviously, compared to P17-E and the pristine Bi_2MoO_6, the resulting 6.7% P-1BMO and 6.7% P-3BMO hybrids demonstrated not only the improved photooxidative ability in CIP decomposition, but also the enhanced photoreductive performance in Cr(VI) removal, indicating the availability of the proposed method to construct highly active organic-inorganic hybrids of different morphologies.

2.4 Insight of the photocatalytic mechanism

As is known to all, surface reactions, solar light harvesting and e^-/h^+ separation speak loudly in photocatalysis. We thus conducted the corresponding measurements to figure out the specific reasons for the enhanced photocatalytic activity over P-BMO composites, especially the most active 6.7% P-2BMO. Figure S10 shows the N_2 adsorption-desorption isotherms of the catalysts, in which all curves complied well with typical Type IV isotherm behavior. All the P-BMO composites exhibited much larger BET surface area than the corresponding pristine Bi_2MoO_6 (Table S1), which could be ascribed to the more dispersive feature of P17-E in the hybrids, just as the TEM images displayed. That is to say more surface active sites might be offered after the hybridization of P17-E and BMO. Nevertheless, P-BMO hybrids still possessed much higher CIP degradation rates after surface area normalization, implying that the increased surface active sites was not the major reason for the boosting photocatalytic activity over P-BMO composites.

The UV-vis absorption spectra were thus measured and displayed in Figure 4a. Compared to the three kinds of pristine Bi_2MoO_6, the corresponding hybrids exhibit much intenser continuous absorption over the Vis-NIR region, which could be attributed to the existence of conjugate structure within P17-E. Based on the plots of $(\alpha h\nu)^{1/2}$ versus photon energy ($h\nu$), the band gap (E_g) of 1BMO, 2BMO and 3BMO were calculated to be 2.61, 2.62 and 2.63 eV, respectively (Figure 4b). In addition, their CB and VB positions were further investigated to analyze their photoredox ability. Figure 4c depicts the Mott−Schottky (MS) plots of the samples, from which the flat band potentials of 1BMO, 2BMO and 3BMO are estimated to be -0.31, -0.26 and -0.24 V versus the Ag/AgCl electrode, respectively. Since the CB potential of the n-type semiconductors are more negative by 0.1 eV than that of the flat band, the CB potentials of 1BMO, 2BMO and 3BMO are calculated to be -0.41, -0.36 and -0.34 V, respectively [46]. Combining with the band gaps, their VB positions are determined to be 2.20, 2.26 and 2.29 V. As for P17-E, its LUMO and HOMO potentials were found to be -0.80 and 1.12 eV in our previous report [29]. For better comparison, the respective data are summarized in Table S2 and displayed in Figure 4d. Obviously, favorable staggered energy band arrangements were obtained between P17-E and Bi_2MoO_6. Combining the tight C-O connection formed in the interface as previous discussed, the separation and migration of photoinduced e^-/h^+ might be significantly promoted.

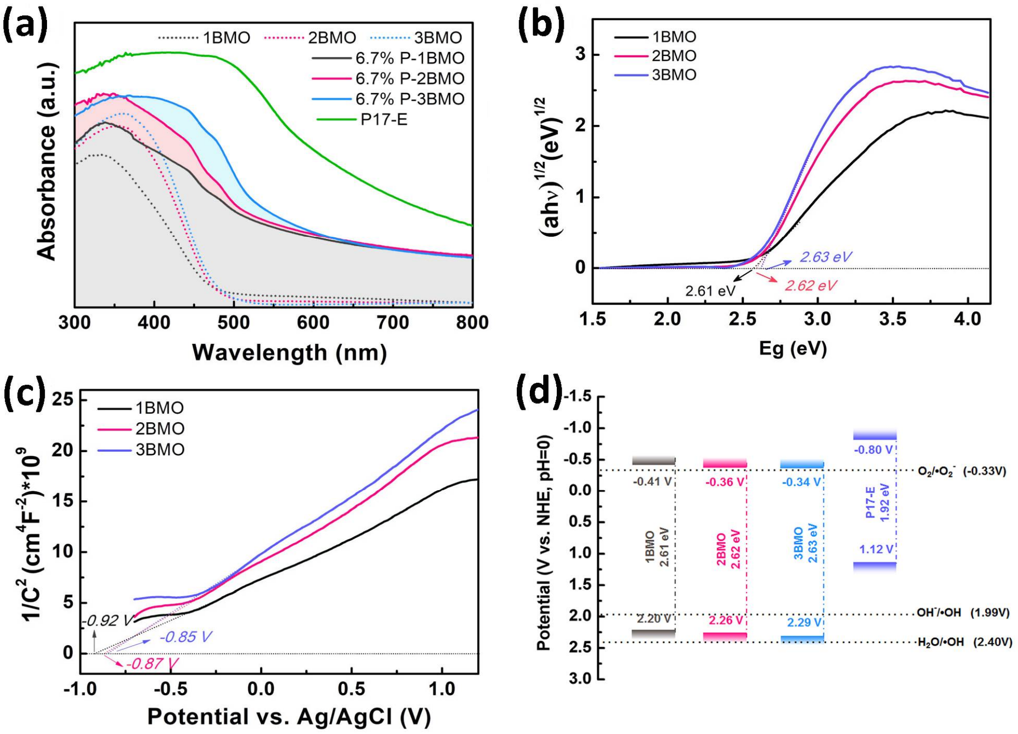

Figure 4. (**a**) UV-vis absorption spectra of all the samples； (**b**) Plots of (αhν)1/2 versus energy *hν*; (**c**) Mott–Schottky plots for 1BMO, 2BMO and 3BMO; (d) The diagram of band positions for 1BMO, 2BMO, 3BMO and P17-E.

Hence, the steady-state photoluminescence (PL) measurements, photocurrent measurements and electrochemical impedance spectra (EIS) were performed for further confirmation. As shown in Figure 5a, all three P-BMO composites display much weaker fluorescence intensity than the corresponding pristine Bi_2MoO_6, implying the construction of effective hybrids can markedly inhibit the recombination of e^-/h^+ pairs. And among all the composites, 6.7% P-2BMO presents the lowest fluorescence intensity, which is in accord with the results of activity tests. Moreover, all the hybrids also exhibit higher photocurrents and smaller semicircle diameters in comparison with 1BMO, 2BMO, 3BMO and P17-E, corresponding to the enhanced separation efficiency and mobility of photoinduced carriers (Figure 5b, c and S11). As such, more active species can participate in the

Peer-reviewed version available at Catalysts 2018, 8, 185; doi:10.3390/catal8050185

catalytic reaction including electrons, holes, $\bullet O_2^-$ and so on, thus enhancing the photocatalytic activity significantly.

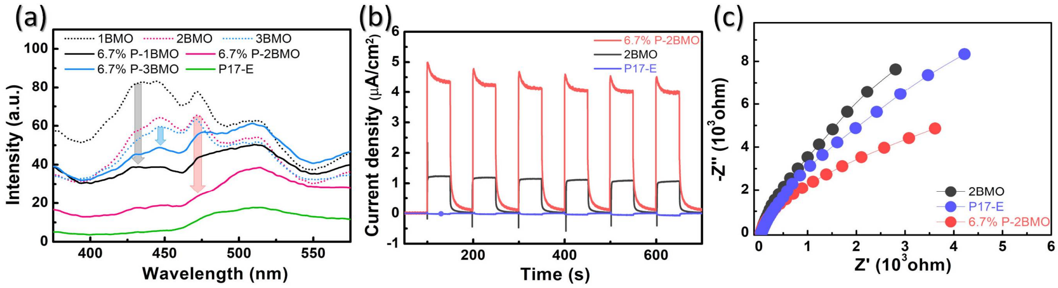

Figure 5. (**a**) PL spectra of all the samples; (**b**) photocurrent response spectra and (**c**) electrochemical impedance spectra of 2BMO, P17-E and 6.7%P-BMO.

The trapping experiments were subsequently conducted to figure out the contribution of the active species during the CIP decomposition over different catalysts. $K_2Cr_2O_7$, TEOA, IPA, SOD and β-carotene were taken as the scavengers for e^-, h^+, •OH, $\bullet O_2^-$ and $^1O_2$, respectively [47]. As displayed in Figure 6, for both 2BMO and 6.7% P-2BMO, the slight decreases of photocatalytic performance with the existence of IPA demonstrated that •OH was not the main active specie in CIP removal. Whereas the remarkable inhibition on CIP degradation caused by TEOA implied the crucial effects of holes on CIP removal for both of them. That was why the photocatalytic activity of 2BMO was obviously improved after $K_2Cr_2O_7$ was added to trap electrons, leaving more holes to degrade CIP. Besides, about 15.9% and 23.5% CIP decomposition were hampered for 2BMO and 6.7% P-2BMO under the presence of SOD, while about 60.3% and 85.3% CIP removal were inhibited for 2BMO and 6.7% P-2BMO after the addition of β-carotene.

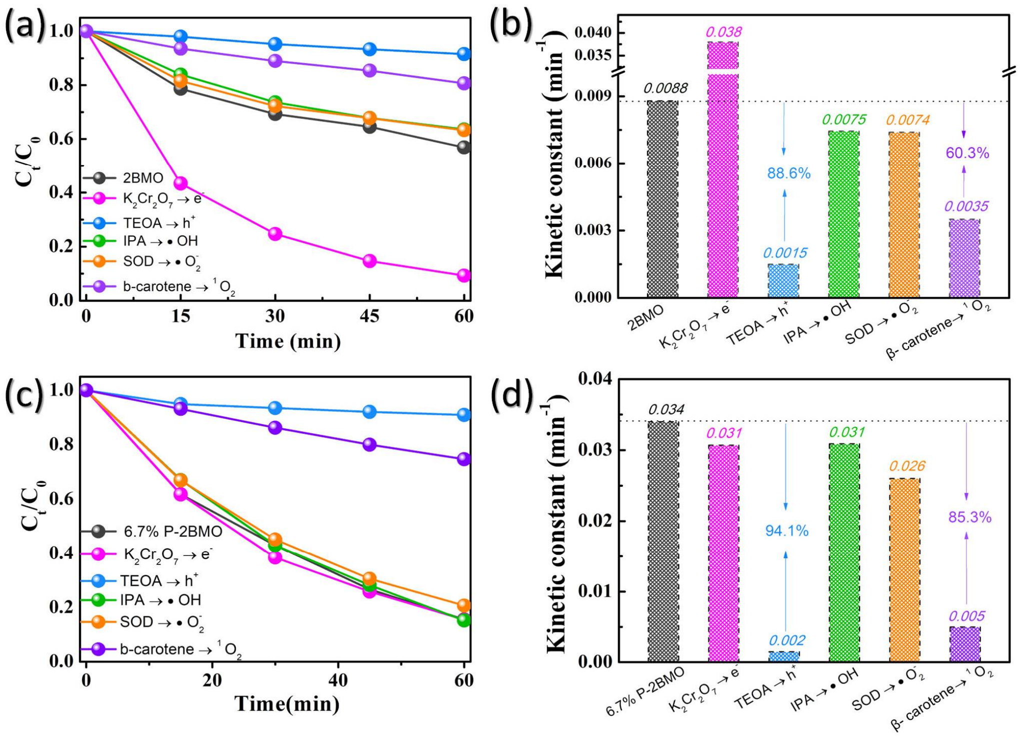

Figure 6. Trapping measurements and the corresponding rate constants for ciprofloxacin photodegradation over 2BMO (**a**, **b**) and 6.7% P-2BMO (**c**, **d**).

These results suggested that •O_2^- and $^1O_2$ were also important active radicals in CIP degradation. And the enhanced inhibition proportions of •O_2^- and $^1O_2$ for 6.7% P-2BMO implied that the modification of Bi_2MoO_6 with P17-E might improve the generation of •O_2^- and $^1O_2$. The similar results were also observed when comparing either 1BMO with 6.7% P-1BMO, or 3BMO with 6.7% P-3BMO (Figure S12-13).

Accordingly, the electron spin resonance (ESR) spectra of 2BMO, P17-E and 6.7% P-2BMO were recorded to confirm this corollary. As expected, the 6.7% P-2BMO hybrid indeed possessed a much higher •O_2^-, $^1O_2$ and •OH generation capability than that of the pristine 2BMO and P17-E after irradiated in visible light for 12 min (Figure 7). As shown in Figure 7a, signals of DMPO-•O_2^- adduct were detected in all samples under visible light irradiation. This is consistent with the previous band position analysis (Figure 4d), because the conduction band potentials of both 2BMO (-0.36 V vs NHE) and P17-E (-0.80 V NHE) are more negative than that of molecule oxygen reduction (O_2/•O_2^-, -0.33 V vs NHE). As the HOMO potential of P17-E (1.12 V) is not positive enough to oxidize H_2O (H_2O/•OH, 2.40 V) or surface hydroxyl (1.99 V), the •OH generated over P17-E might be derived from the reaction of •O_2^- via •O_2^-→H_2O_2→•OH process (Figure 7c) [48-50].

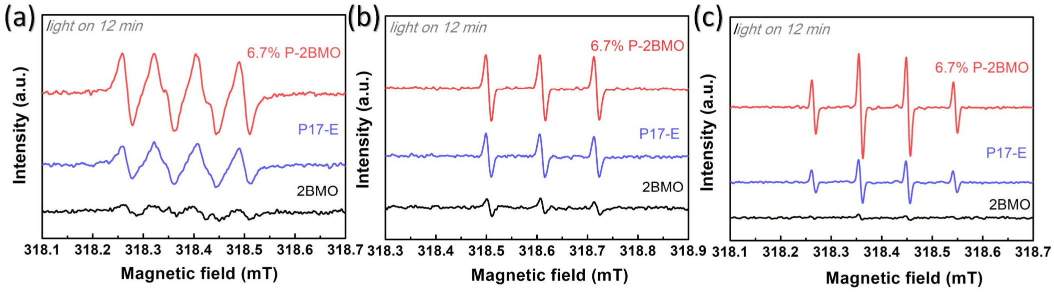

Figure 7. ESR spectra of DMPO-•O_2^- (**a**), TEMP-$^1O_2$ (**b**) and DMPO-•OH (**c**).

For better confirmation, quantitative determination of •O_2^- and •OH over 2BMO, P17-E and 6.7% P-2BMO were thus conducted through the NBT photodegradation and TA photoluminescence (PL) tests under visible light irradiation (Figure 8 and S14, 15). As displayed in Figure 8a, •O_2^- accumulation was found for all samples under the visible light irradiation. Among of them, the 6.7% P-2BMO possesses the highest •O_2^- concentration (28.2 μmol/L) in three hours, which agrees well with the ESR results. During the whole •OH determination tests, N_2 was bubbled in the solution to exclude •O_2^-→H_2O_2→•OH path. As can be seen in Figure 8b, an obvious •OH generation was found for 2BMO in visible light without the involvement of O_2, confirming that 2BMO can directly oxidize surface hydroxyl to •OH. As for P17-E, almost no •OH was accumulated in three hours under visible light irradiation after O_2 was excluded by N_2, in line with expectations, thereby verifying that the •OH detected by ESR result from the transformation of •O_2^-. Intriguingly, the 6.7% P-2BMO can also oxidize the surface hydroxyl and generate more •OH in comparison with 2BMO. That is to say the P-BMO hybrids conserved the stronger oxidizing ability of BMO and the higher reducing ability of P17-E as well, so we deduce that the electron transfer mode of P-BMO is Z-scheme rather than the conventional type II (Figure 8c). This was further confirmed by Pt photodeposition experiments. From the HRTEM images of Pt nanoparticles (NPs) decorated 6.7% P-2BMO (Figure 8d-f), most of the Pt NPs with clear characteristic lattice fringe corresponding to Pt(111) plane are observed on the surface of P17-E rather than Bi_2MoO_6 nanosheets. As Pt NPs are inclined to deposit and accumulate around electron-rich sites because of the electrophilic nature of Pt^{4+} species [39], it can be inferred that the electrons are transported form CB of 2BMO to the HOMO of P17-E through Z-scheme mechanism and thus reduced the Pt (IV) to Pt NPs on the surface of P17-E. Combining the results above, the Z-scheme mechanism was proved to be reasonable, validating the availability of the proposed strategy to construct Z-scheme organic-inorganic hybrids with enhanced photocatalytic performance.

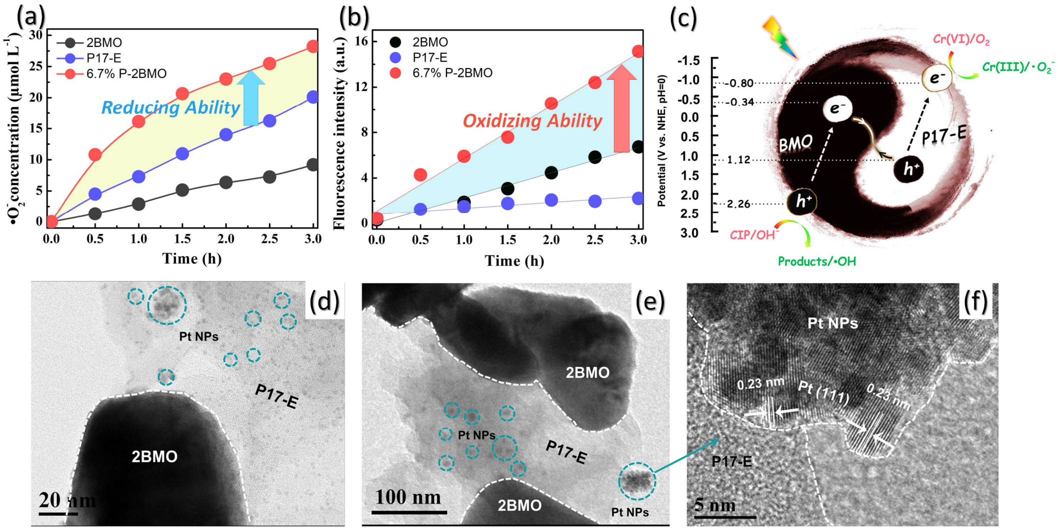

Figure 8. Quantitative determination of $\bullet O_2^-$ (**a**) and •OH (**b**) generation for 2BMO, 6.7% P-2BMO and P17-E; (**c**) Proposed photocatalytic mechanism of P-BMO according to Z-scheme electron transfer mode; (**d-f**) TEM and corresponding HRTEM images of 6.7% P-2BMO hybrid after in-situ photodeposition of Pt from H_2PtCl_6.

3. Materials and Methods

3.1 Materials

Bismuth nitrate ($Bi(NO_3)_3{\cdot}5H_2O$), sodium molybdate ($Na_2MoO_4{\cdot}2H_2O$), oleylamine, nitric acid, ammonia, ethylene glycol, *N*, *N*-Dimethylformamide (DMF), triethylamine (TEA), methanol (MeOH), dichloromethane (CH_2Cl_2) and copper(I) iodide (CuI) were purchased from Sinopharm Chemical Reagent Corp. (China). Bis(triphenylphosphine)palladium(II) chloride ($Pd(PPh_3)_2Cl_2$) was obtained from Energy Chemical. 1,6-Dibromopyrene and 1,4-diethynylbenzene were supplied by Shanghai Bepharm Corporation. All of the reagents were analytically pure level and used as received without further purification. Deionized water was used throughout the synthesis.

3.2 Preparation of photocatalysts

The pristine conjugated polymer P17-E was synthesized via the Sonogashira-Hagihara cross-coupling reaction following our previous report [29]. The Bi_2MoO_6 nanosheets (2BMO) were synthesized via a facile hydrothermal process. Typically, 2 mmol $Bi(NO_3)_3{\cdot}5H_2O$ was dissolved in 20 mL nitric acid solution (2 M). Then 10 mL Na_2MoO_4 solution (0.1 M) was added to the above solution under vigorous magnetic stirring. After that, the pH value of the system was adjusted to 7 with concentrated ammonia. The obtained light-yellow suspension was transferred into Teflon-lined stainless steel autoclave, and heated at 180 °C for 24 h. Finally, the resultant precipitates were collected, washed with deionized water and ethanol, and dried at 80 °C overnight.

The P-2BMO hybrids were fabricated by in-situ polycondensation of P17-E in the presence of Bi_2MoO_6 nanosheets. As schematically illustrated in Scheme S1, a schlenk tube was charged with Bi_2MoO_6, 1,6-Dibromopyrene, 1,4-diethynylbenzene, $Pd(PPh_3)_2Cl_2$, CuI and 10 mL mixed solvent (DMF/TEA = 1/1). The resulting mixture was then stirred at 80 °C for 24 h under Ar atmosphere. After that, the obtained brown precipitate was filtered off, washed in the Soxhlet extractor containing mixed solvent of DCM/MeOH for about 48 hours and dried at 60 °C overnight. Moreover, in order to determine the optimum P17-E amount in the hybrids, a series of P-2BMO with different weight ratio were synthesized and labeled as 3.3%, 6.7%, 10%, and 16.7% P-2BMO (x% means the mass ratio of P17-E to Bi_2MoO_6 nanosheets on condition that the precursors are converted completely).

Peer-reviewed version available at *Catalysts* **2018**, *8*, 185; doi:10.3390/catal8050185

3.3 Characterizations

X-ray diffraction (XRD) patterns were recorded through an X-ray diffractometer equipped with Cu Kα radiation (D8 advance Bruker Inc., Germany). Raman spectra were acquired on a DXR Raman Microscope (Thermo Fisher, USA). Fourier transform infrared spectra (FT-IR) were measured on a Nicolet iS50 FT-IR spectrometer (Thermo Fisher, USA).Transmission electron microscopy (TEM) images were recorded on JEM-2010 (JEOL, Japan). High-resolution transmission electron microscopy (HRTEM) imaging was carried out on a Tecnai G2 F20 S-TWIN microscope (FEI, USA) operated at 200 kV. X-ray photoelectron spectroscopy (XPS) tests were operated on ESCALAB 250Xi system (Thermo Fisher, America), and all binding energies were referenced to the C 1s peak at 284.4 eV of the surface adventitious carbon. Diffuse reflection spectra (DRS) were acquired using a PerkinElmer lambda 650s UV/vis spectrometer. The photoluminescence (PL) measurements were conducted on PerkinElmer LS55 fluorescence spectrometer using 325 nm as excitation wavelength. Brunauer-Emmett-Teller (BET) specific surface area was estimated on a nitrogen adsorption- desorption apparatus (ASAP 2040, Micrometrics Inc., USA) with all samples degassed at 100 ^{o}C for 12 h prior to measurements. Thermogravimetric (TG) analysis was performed in air atmosphere through a thermal gravimetric analyzer (TG209, NETZSCH Inc., Germany) with the temperature increased from 30 to 800 ^{o}C with a heating rate of 10 ^{o}C•min^{-1}.

3.4 Measurement of photocatalytic activity

The visible-light photocatalytic performance of the prepared catalysts were systematically evaluated by the photoremoval of ciprofloxacin (CIP) and toxic Cr (IV). A 300 W Xe lamp (PLS SXE300, Beijing Perfectlight Inc., China) was served as the simulated solar light source with a light filter ($\lambda \geq 420$ nm) to eliminate UV light. For CIP photodegradation, 20 mg of the photocatalyst was dispersed in an aqueous solution of CIP (50 mL, 20 ppm). Prior to irradiation, the suspension was continuously stirred in dark for 1 h to establish adsorption-desorption equilibrium. During the illumination, about 3 mL aliquots was sampled from the reactor at the interval 15 min over 60 min, followed by filtration to remove the solid. The concentration of CIP was determined by HPLC equipped with an Agilent TC-C18 column and a UV Detector at 275 nm. The stability of the photocatalysts was evaluated through the recycling experiments. After each reaction, the photocatalyst was collected by centrifugation, washed, dried, and then used for the next run.

Similar to the CIP photodegradation, the photoreduction of toxic Cr(IV) was carried out as follows: 50 mg photocatalyst was suspended in an aqueous solution of Cr(IV) (50 mL, 20 ppm) and 0.01 M HCl. After the adsorption equilibrium in dark, about 4 mL aliquots were collected and centrifuged at given intervals during the irradiation. The concentration of Cr(IV) was evaluated via the standard diphenylcarbazide (DPC) method with a Shimadzu UV-Vis spectrophotometer.

3.5 Detection of reactive species

For the trapping experiments, various scavengers were added into the ciprofloxacin aqueous solution to capture the corresponding active species. In briefly, $K_2Cr_2O_7$, triethanolamine (TEOA), isopropanol (IPA), superoxide dismutase (SOD) and natural β-carotene served as electron, hole, •OH, $•O_2^-$ and $^1O_2$ scavengers, respectively. Electron paramagnetic resonance spectroscopy with 5,5-Dimethyl-1-pyrroline-N-oxide (DMPO)-methanol, DMPO, and 2,2,6,6-tetramethylpiperidine (TEMP) as trapping agent in situ trap the spin-reactive species were used to detect the $•O_2^-$, •OH and $^1O_2$, respectively. The amount of $•O_2^-$ was quantitatively analyzed by measuring the wastage of nitroblue tetrazolium (NBT, 2×10^{-5} mol•L^{-1}) on a UV–vis spectrophotometer at 259 nm, while the generation of •OH was quantified by detecting the concentration of 2-OH-terephthalic acid, generated from the reaction of terephthalic acid (TA, 5×10^{-4} mol L^{-1} in a 2×10^{-3} mol L^{-1} NaOH solution) with •OH, using a fluorescence spectrophotometer with excitation wavelength at 312 nm.

3.6 Photoelectrochemical measurements

All the photoelectrochemical experiments including C-V test, photocurrent, electrochemical impedance spectra (EIS) and Mott–Schottky (M-S) measurements were performed on CHI 660D electrochemical work station (Chenhua Instrument, Shanghai, China). A platinum foil and Ag/AgCl (saturated KCl) were utilized as the counter electrode and reference electrode, respectively. For the C-V test, the glassy carbon electrode was applied as the working electrode with 0.1 M $TBAPF_6$ in acetonitrile as the electrolyte. For the other measurements, the working electrodes were prepared as our previous paper [27]. And 0.1 M Na_2SO_4 aqueous solution was used as the electrolyte in photocurrent and M-S measurements, while the electrolyte in EIS test is the mixture solution of 0.1 M KCl and 0.5 mM $K_3[Fe(CN)_6]$. In addition, a 300 W Xe lamp (PLS SXE300, Beijing Perfectlight Inc., China) was utilized as the light source during the photocurrent measurement.

4. Conclusions

In summary, the original organic-inorganic Z-scheme hybrids (P-BMO) were designed and synthesized via the in-situ cross-coupling reaction. The incorporation of P17-E into inorganic semiconductor (Bi_2MoO_6) was proved to be a feasible strategy to enhance both the photooxidation and photoreduction activity of Bi_2MoO_6. Characterization results demonstrated that the enhanced performance can be attributed to the wider visible light absorption, higher e^-/h^+ separation and larger surface area. In line with the results of photoelectrochemical measurements and trapping tests, the reasonable Z-scheme mechanism was proposed and verified via the determination of reactive species ($\bullet O_2^-$ and $\bullet OH$) and Pt nanoparticles photodeposition experiments. This work taking different dimensional Bi_2MoO_6 as the model materials, provides an available strategy to construct Z-scheme organic-inorganic hybrid photocatalysts with enhanced photocatalytic performance.

Supplementary Materials: The following are available online at www.mdpi.com/link, Scheme S1: In situ generation of P17-E on the surface of different dimensional Bi_2MoO_6. Figure S1: FT-IR spectra of 2BMO, 6.7% P-2BMO and P17-E; Figure S2: (a) XPS spectra of Bi 4f (b) and Mo 3d; Figure S3: TG analysis of 2BMO, 6.7% P-2BMO and P17-E; Figure S4: XRD patterns of 1BMO, 3BMO, 6.7% P-1BMO, 6.7% P-3BMO and P17-E; Figure S5: TEM images of 1BMO (a), 6.7% P-1BMO (b), 3BMO (c) and 6.7% P-3BMO (d), inset shows the corresponding HRTEM images; Figure S6: FT-IR spectra of 1BMO, 3BMO, 6.7% P-1BMO, 6.7% P-3BMO and P17-E; Figure S7: Raman spectra of 1BMO, 3BMO, 6.7% P-1BMO, 6.7% P-3BMO and P17-E; Figure S8: TG analysis of 1BMO, 3BMO, 6.7% P-1BMO, 6.7% P-3BMO and P17-E; Figure S9: Photodegradation of ciprofloxacin (a) and photoreduction of Cr(VI) (b) over 1BMO, 3BMO, 6.7% P-1BMO, 6.7% P-3BMO and P17-E; Figure S10: N_2-adsorption-desorption isotherms of all the samples; Figure S11: photocurrent response spectra (a) and electrochemical impedance spectra (b) of all the samples; Figure S12: Trapping measurements and the corresponding rate constants for ciprofloxacin photodegradation over1BMO (a, b) and 6.7% P-1BMO (c, d); Figure S13: Trapping measurements and the corresponding rate constants for ciprofloxacin photodegradation over 3BMO (a, b) and 6.7% P-3BMO (c, d); Figure S14: Spectra of NBT transformation generated by 2BMO (a), P17-E (b) and 6.7% P-2BMO (c) under visible light irradiation. Table S1: BET surface areas of all the samples; Table S2: The analysis of band positions for 1BMO, 2BMO and 3BMO.

Acknowledgments: This work was financially supported by National Natural Science Foundation of China (21607047, 51572101), Natural Science Foundation of Hubei Province (2016CFB193) and Fundamental Research Funds for the Central Universities (2662015QD047, 2662016PY088).

Author Contributions: In this paper, Xing Ding and Hao Chen designed the experiments; Xianglong Yang and Yonggang Xiang conducted the experiments; Xuepeng Wang and Shu Li analyzed the data; Xianglong Yang and Xing Ding wrote the paper.

Conflicts of Interest: The authors declare no conflict of interest.

References

1. Marin, M.L.; Santos-Juanes, L.; Arques, A.; Amat, A.M.; Miranda, M.A. Organic photocatalysts for the oxidation of pollutants and model compounds. *Chem. Rev.* **2012**, *112*, 1710-1750.
2. Schneider, J.; Matsuoka, M.; Takeuchi, M.; Zhang, J.; Horiuchi, Y.; Anpo, M.; Bahnemann, D.W. Understanding TiO_2 photocatalysis: mechanisms and materials. *Chem. Rev.* **2014**, *114*, 9919-9986.

3. Alex, O.I.; Paul, F. Heterogeneous photocatalysis: recent advances and applications. *Catalysts* **2013**, *3*, 189-218.
4. Li, X.; Yu, J.; Jaroniec, M. Hierarchical photocatalysts. *Chem. Soc. Rev.* **2016**, *45*, 2603-2636.
5. Zhang, X.; Peng, T.; Song, S. Recent advances in dye-sensitized semiconductor systems for photocatalytic hydrogen production. *J. Mater. Chem. A* **2016**, *4*, 2365-2402.
6. Zhang, H.; Lin, C.; Han, T; Du, F.; Zhao, Y.; Li, X.; Sun Y. Visualization of the formation and 3D porous structure of Ag doped MnO_2 aerogel monoliths with high photocatalytic activity. *ACS Sustainable Chem. Eng.* **2016**, *4*, 6277-6287.
7. Low, J.; Yu, M.; Jaroniec, M.; Wageh, S.; Al-Ghamdi, A.A. Heterojunction photocatalysts. *Adv. Mater.* **2017**, *29*, 1601694.
8. Li, H.; Li, J.; Ai, Z.; Jia, F.; Zhang, L. Oxygen vacancy-mediated photocatalysis of BiOCl: reactivity, selectivity, and perspectives. *Angew. Chem. Int. Ed.* **2018**, *57*, 122-138.
9. Jiao, X.; Chen, Z.; Li, X.; Sun, Y.; Gao, S.; Yan, W.; Wang, C.; Zhang, Q.; Lin, Y.; Luo, Y.; Xie, Y. Defect-mediated electron-hole separation in one-unit-cell $ZnIn_2S_4$ layers for boosted solar-driven CO_2 reduction. *J. Am. Chem. Soc.* **2017**, *139*, 7586-7594.
10. He, Y.; Zhang, L.; Teng, B.; Fan, M. New application of Z-scheme Ag_3PO_4/g-C_3N_4 composite in converting CO_2 to fuel. *Environ. Sci. Technol.* **2015**, *49*, 649-656.
11. Zhou, P.; Yu, J.; Jaroniec, M. All-solid-state Z-scheme photocatalytic systems. *Adv. Mater.* **2014**, *26*, 4920-4935.
12. Miao, X.; Shen, X.; Wu, J.; Ji, Z.; Wang, J.; Kong, L.; Liu, M.; Song, C. Fabrication of an all solid Z-scheme photocatalyst g-C_3N_4/GO/AgBr with enhanced visible light photocatalytic activity. *Appl. Catal. A* **2017**, *539*, 104-113.
13. Xia, P.; Zhu, B.; Cheng, B.; Yu, J.; Xu, J. 2D/2D g-C_3N_4/MnO_2 nanocomposite as a direct Z-scheme photocatalyst for enhanced photocatalytic activity. *ACS Sustainable Chem. Eng.* **2018**, *6*, 965-973.
14. Zhang, Z.; Huang, J.; Fang, Y.; Zhang, M.; Liu, K.; Dong, B. A nonmetal plasmonic Z-Scheme Photocatalyst with UV- to NIR-driven photocatalytic protons reduction. *Adv. Mater.* **2017**, *29*, 1606688.
15. Hong, Y.; Jiang, Y.; Li, C.; Fan, W.; Yan, X.; Yan, M.; Shi, W. In-situ synthesis of direct solid-state Z-scheme V_2O_5/g-C_3N_4 heterojunctions with enhanced visible light efficiency in photocatalytic degradation of pollutants. *Appl. Catal. B* **2016**, *180*, 663-673.
16. Li, H.; Hu, T.; Zhang, R.; Liu, J.; Hou, W. Preparation of solid-state Z-scheme Bi_2MoO_6/MO (M = Cu, $Co_{3/4}$, or Ni) heterojunctions with internal electric field-improved performance in photocatalysis. *Appl. Catal. B* **2016**, *188*, 313-323.
17. Lin, Y.; Zhao, F.; He, Q.; Huo, L.; Wu, Y.; Parker, T.C.; Ma, W.; Sun, Y.; Wang, C.; Zhu, D.; Heeger, A.J.; Marder, S.R.; Zhan, X. High-performance electron acceptor with thienyl side chains for organic photovoltaics. *J. Am. Chem. Soc.* **2016**, *138*, 4955-4961.
18. Sun, C.; Wu, Z.; Yip, H.; Zhang, H.; Jiang, X.; Xue, Q.; Hu, Z.; Hu, Z.; Shen, Y.; Wang, M.; Huang, F.; Cao, Y. Amino-functionalized conjugated polymer as an efficient electron transport layer for high-performance planar-heterojunction perovskite solar cells. *Adv. Energy. Mater.* **2016**, *6*, 1501534.
19. Liu, C.; Wang, K.; Gong, X.; Heeger, A.J. Low bandgap semiconducting polymers for polymeric photovoltaics. *Chem. Soc. Rev.* **2016**, *45*, 4825-4846.
20. Zhang, K.; Kopetzki, D.; Seeberger, P.H.; Antonietti, M.; Vilela, F. Surface area control and photocatalytic activity of conjugated microporous poly(benzothiadiazole) networks. *Angew. Chem. Int. Ed.* **2013**, *52*, 1432-1436.
21. Cui, C.; He, Z.; Wu, Y.; Cheng, X.; Wu, H.; Li, Y.; Cao, Y.; Wong, W. High-performance polymer solar cells based on a 2D-conjugated polymer with an alkylthio side-chain. *Energy Environ. Sci.* **2016**, *9*, 885-891.
22. Ghosh, S.; Kouamé, N.A.; Ramos, L.; Remita, S.; Dazzi, A.; Deniset-Besseau, A.; Beaunier, P.; Goubard, F.; Aubert, P.; Remita, H. Conducting polymer nanostructures for photocatalysis under visible light. *Nature Mater.* **2015**, *14*, 505-511.
23. Yang, C.; Ma, B.C.; Zhang, L.; Lin, S.; Ghasimi, S.; Landfester, K.; Zhang, K.A.; Wang, X. Molecular engineering of conjugated polybenzothiadiazoles for enhanced hydrogen production by photosynthesis. *Angew. Chem. Int. Ed.* **2016**, *55*, 9202-9206.
24. Xiang, Y.; Zhang, X.; Wang, X.; Ding, X.; Huang, D.; Chen, H. Molecular structure design of conjugated microporous poly(dibenzo[b, d]thiophene 5,5-dioxide) for optimized photocatalytic NO removal. *J. Catal.* **2018**, *357*, 188-194.

25. Sprick, R.S.; Jiang, J.X.; Bonillo, B.; Ren, S.; Ratvijitvech, T.; Guiglion, P.; Zwijnenburg, M.A.; Adams, D.J.; Cooper, A.I. Tunable organic photocatalysts for visible-light-driven hydrogen evolution. *J. Am. Chem. Soc.* **2015**, *137*, 3265-3270.
26. Lan, Z.A.; Fang, Y.; Zhang, Y.; Wang, X. Photocatalytic oxygen evolution from functional triazine-based polymers with tunable band structures. *Angew. Chem. Int. Ed.* **2018**, *57*, 470-474.
27. Yang, X.; Xiang, Y.; Qu, Y.; Ding, X.; Chen, H. Novel in situ fabrication of conjugated microporous poly(benzothiadiazole)-Bi_2MoO_6 Z-scheme heterojunction with enhanced visible light photocatalytic activity. *J. Catal.* **2017**, *345*, 319-328.
28. Zhang, X.; Xiao, J.; Hou, M.; Xiang, Y.; Chen, H. Robust visible/near-infrared light driven hydrogen generation over Z-scheme conjugated polymer/CdS hybrid. *Appl. Catal. B* **2018**, *224*, 871-876.
29. Zhang, X.; Wang, X.; Xiao, J.; Wang, S.; Huang, D.; Ding, X.; Xiang, Y.; Chen, H. Synthesis of 1,4-diethynylbenzene-based conjugated polymer photocatalysts and their enhanced visible/near-infrared-light-driven hydrogen production activity. *J. Catal.* **2017**, *350*, 64-71.
30. Zhang, L.; Xu, T.; Zhao, X.; Zhu, Y. Controllable synthesis of Bi_2MoO_6 and effect of morphology and variation in local structure on photocatalytic activities. *Appl. Catal. B* **2010**, *98*, 138-146.
31. Wang, S.; Ding, X.; Zhang, X.; Pang, H.; Hai, X.; Zhan, G.; Zhou, W.; Song, H.; Zhang, L.; Chen, H.; Ye, J. In situ carbon homogeneous doping on ultrathin bismuth molybdate: A dual-purpose strategy for efficient molecular oxygen activation. *Adv. Funct. Mater.* **2017**, *27*, 1703923.
32. Li, H.; Liu, J.; Hou, W.; Du, N.; Zhang, R.; Tao, X. Synthesis and charactserization of g-C_3N_4/Bi_2MoO_6 heterojunctions with enhanced visible light photocatalytic activity. *Appl. Catal. B* **2014**, *160*, 89-97.
33. Tian, J.; Hao, P.; Wei, N.; Cui, H.; Liu, H. 3D Bi_2MoO_6 nanosheet/TiO_2 nanobelt heterostructure: enhanced photocatalytic activities and photoelectochemistry performance. *ACS. Catal.* **2015**, *5*, 4530-4536.
34. Dai, W.; Yu, J.; Xu, H.; Hu, X.; Luo, X.; Yang, L.; Tu, X. Synthesis of hierarchical flower-like Bi_2MoO_6 microspheres as efficient photocatalyst for photoreduction of CO_2 into solar fuels under visible light. *CrystEngComm* **2016**, *18*, 3472-3480.
35. Di, J.; Xia, J.; Ji, M.; Li, H.; Xu, H.; Li, H.; Chen, R. The synergistic role of carbon quantum dots for the improved photocatalytic performance of Bi_2MoO_6. *Nanoscale* **2015**, *7*, 11433-11443.
36. Sun, S.; Wang, W. Advanced chemical compositions and nanoarchitectures of bismuth based complex oxides for solar photocatalytic application. *RSC Adv.* **2014**, *4*, 47136-47152.
37. Tian, N.; Huang, H.; He, Y.; Guo, Y.; Zhang, T.; Zhang, Y. Mediator-free direct Z-scheme photocatalytic system: $BiVO_4$/g-C_3N_4 organic-inorganic hybrid photocatalyst with highly efficient visible-light-induced photocatalytic activity. *Dalton Trans* **2015**, *44*, 4297-4307.
38. Kumar, S.; Baruah, A.; Tonda, S.; Kumar, B.; Shanker, V.; Sreedhar, B. Cost-effective and eco-friendly synthesis of novel and stable N-doped ZnO/g-C_3N_4 core-shell nanoplates with excellent visible-light responsive photocatalysis. *Nanoscale* **2014**, *6*, 4830-4842.
39. Li, X.; Xie, K.; Song, L.; Zhao, M.; Zhang, Z. Enhanced photocarrier separation in hierarchical graphitic-C_3N_4-supported $CuInS_2$ for noble-metal-free Z scheme photocatalytic water splitting. *ACS Appl Mater Interfaces* **2017**, *9*, 24577-24583.
40. Bai, X.; Sun, C.; Wu, S.; Zhu, Y. Enhancement of photocatalytic performance via a P3HT-g-C_3N_4 heterojunction. *J. Mater. Chem. A* **2015**, *3*, 2741-2747.
41. Kongmark, C.; Martis, V.; Pirovano, C.; Löfberg, A.; Beek, W.; Sankar, G.; Rubbens, A.; Cristol, S.; Vannier, R.N.; Bordes-Richard, E. Synthesis of γ-Bi_2MoO_6 catalyst studied by combined high-resolution powder diffraction, XANES and Raman spectroscopy. *Catal. Today* **2010**, *157*, 257-262.
42. Ding, X.; Ho, W.; Shang, J.; Zhang, L. Self doping promoted photocatalytic removal of no under visible light with Bi_2MoO_6: Indispensable role of superoxide ions. *Appl. Catal. B* **2016**, *182*, 316-325.
43. Hull, R.V.; Li, L.; Xing, Y.; Chusuei, C.C. Pt nanoparticle binding on functionalized multiwalled carbon nanotubes. *Chem. Mater.* **2006**, *18*, 1780-1788.
44. Kovtyukhova, N.I.; Mallouk, T.E.; Pan, L.; Dickey, E.C. Individual single-walled nanotubes and hydrogels made by oxidative exfoliation of carbon nanotube Ropes. *J. Am. Chem. Soc.* **2003**, *1252*, 9761-9769.
45. Wen, X.; Niu, C.; Zhang, L.; Liang, C.; Guo, H.; Zeng, G. Photocatalytic degradation of ciprofloxacin by a novel Z-scheme CeO_2-Ag/AgBr photocatalyst: Influencing factors, possible degradation pathways, and mechanism insight. *J. Catal.* **2018**, *358*, 141-154.
46. Bai, Y.; Ye, L.; Chen, T.; Wang, L.; Shi, X.; Zhang, X.; Chen, D. Facet-dependent photocatalytic N_2 fixation of bismuth-rich Bi_5O_7I nanosheets. *ACS Appl Mater Interfaces* **2016**, *8*, 27661-27668.

Peer-reviewed version available at *Catalysts* **2018**, *8*, 185; doi:10.3390/catal8050185

47. Ding, X.; Zhao, K.; Zhang, L. Enhanced photocatalytic removal of sodium pentachlorophenate with self-doped Bi_2WO_6 under visible light by generating more superoxide ions. *Environ. Sci. Technol.* **2014**, *48*, 5823-5831.
48. Wang, D.; Zhao, L.; Ma, H.; Zhang, H.; Guo, L.H. Quantitative analysis of reactive oxygen species photogenerated on metal oxide nanoparticles and their bacteria toxicity: the role of superoxide radicals. *Environ. Sci. Technol.* **2017**, *51*, 10137-10145.
49. Wang, H.; Chen, S.; Yong, D.; Zhang, X.; Li, S.; Shao, W.; Sun, X.; Pan, B.; Xie, Y. Giant electron-hole interactions in confined layered structures for molecular oxygen activation. *J. Am. Chem. Soc.* **2017**, *139*, 4737-4742.
50. Dong, F.; Wang, Z.; Li, Y.; Ho, W.K.; Lee, S.C. Immobilization of polymeric g-C_3N_4 on structured ceramic foam for efficient visible light photocatalytic air purification with real indoor illumination. *Environ. Sci. Technol.* **2014**, *48*, 10345-10353.